Revealing the degree and impact of inhomogeneous electrolyte distributions on silver based gas diffusion electrodes

Maximilian Röhe[a,b], David Franzen[c], Fabian Kubannek[a], Barbara Ellendorff[c], Thomas Turek[c], Ulrike Krewer[b,*]

[a] Institute of Energy and Process Systems Engineering, Technische Universität Braunschweig, Langer Kamp 19b, Braunschweig 38106, Germany
[b] Institute for Applied Materials – Electrochemical Technologies, Karlsruhe Institute of Technology, Adenauerring 20b, Karlsruhe 76131, Germany
[c] Institute of Chemical and Electrochemical Process Engineering, Technische Universität Clausthal, Leibnizstr. 17, Clausthal-Zellerfeld 38678, Germany

Keywords:
Oxygen reduction reaction
Electrochemical impedance spectroscopy
Local inhomogeneities
Mass transfer effects
Maxwell-Stefan diffusion

A B S T R A C T

Silver based oxygen depolarized cathodes (ODC) are a promising technology to reduce the specific electrical energy demand of chlor-alkali electrolysis by around 30 %. Here we present the first modeling approach of an ODC for evaluating the influence of inhomogeneities on electrochemical performance and electrode dynamics. The focus is laid on the electrolyte distribution in the electrode because it is crucial for the gas-electrolyte interface and thus electrode performance and dynamics. To model the inhomogeneities, several one-dimensional three-phase models with different flooding degree of the electrode are coupled in parallel. The model is validated against polarization curves and electrochemical impedance spectra for ODC with silver content of 92, 97, 98 and 99 wt-% Ag. The electrochemical impedance spectroscopy measurements show flattened semicircles in the Nyquist plot with one apparent fast time constant, which ranges from 0.0015 s to 0.03 s depending on the respective ODC composition. The fast time constants result from electrochemical reaction and double layer; no time constant for a mass transport was identified. According to the simulations, the distorted form of the semi-circles is caused by local distribution of the liquid electrolyte within the ODC. It is revealed that there are strong gradients in local performance inside the electrode. Domains with a low intrusion of liquid electrolyte seem to be electrochemically highly active whereas flooded domains are almost inactive. The comparison of ODC with varying silver/polytetrafluoroethylene ratio suggests that the size and location of the gas-liquid interface, rather than the wetted catalyst surface area, is the key to achieving high ODC performance. We reveal that the electrochemical impedance spectroscopy is sensitive to the electrolyte distribution, while polarization curves do not contain sufficient information about the location and distribution of the electrolyte.

1. Introduction

The alkaline oxygen reduction reaction (ORR), Eq. (1), plays a key role in many different electrochemical applications – such as fuel cells, metal-air batteries or a new generation of industrial-scale chlor-alkali electrolyzers [1].

$$O_2 + 2H_2O + 4e^- \rightarrow 4OH^- \quad (1)$$

In the latter example, the ORR is of particular importance: In the advanced chlor-alkali electrolysis, oxygen depolarized cathodes (ODC) are used to reduce oxygen to hydroxide, instead of producing hydrogen. This decreases the needed cell voltage by about 1V and therefore the demand of electrical energy by around 30% [2].

Typically, silver is used as a catalyst in ODC, as it has a high catalytic activity for the ORR that is comparable to platinum when operating under industrial conditions [3] of NaOH-electrolyte concentrations exceeding 10 M and temperatures of 80 to 90 °C [4]. Since the oxygen solubility in the electrolyte is very poor at these conditions [5], a large interface between liquid electrolyte and gaseous oxygen is needed to overcome the mass transport limitation due to the absence of oxygen in the liquid phase [6] and to ensure the required current densities of 4 to 6 kA m^{-2} [7]. Therefore, ODC are realised as porous gas diffusion electrodes (GDE). To form a large interface between the liquid and the gaseous phase, ODC contain hydrophobic polytetrafluoroethylene (PTFE) as second component in addition to the hydrophilic silver. This prevents a complete flooding of the ODC by the liquid electrolyte. As stated recently, the ratio of PTFE and silver of utmost importance for the electrode performance. In their experimental study, Franzen et al. [8] analyzed ten ODC with a silver content of 90 to 99 wt-% (10 to

* Corresponding author.
E-mail address: ulrike.krewer@kit.edu (U. Krewer).

List of Symbols

$A_{\text{geometrical}}$	Geometrical electrode Area (m^2)
a_i	Activity of species i (−)
b_i	Molality of species i (mol kg^{-1})
C_{dl}	Double layer capacitance (F m^{-2})
c_i	Concentration of species i (mol m^{-3})
$\mathscr{D}_{ij}$	Binary Fick's diffusion coefficient for species i and j (m^2 s^{-1})
$Đ_{ij}$	Binary Maxwell-Stefan diffusion coefficient for species i and j ($m^2 s^{-1}$)
E	Potential (V)
E_0	Open circuit potential (V)
E_{00}	Standard electrode potential (V)
F	Faraday constant (= 96485.34) (C mol^{-1})
f	Frequency (s^{-1})
H_i	(Inverse) Henry constant of species i (Pa m^3 mol^{-1})
j	Current density (A m^{-2})
k_0	Reaction rate constant (mol s^{-1})
$\dot{N}_i$	Mass flow density of species i (mol s^{-1} m^{-2})
p	Pressure (Pa)
p_i	Partial pressure of species i (Pa)
p_v	Proportion of the flooded pore volume (−)
R	Universal gas constant (= 8.3145) (J mol^{-1} K^{-1})
R_{specific}	Specific resistance (Ω m^2)
R_{CT}	Charge transfer resistance (Ω)
r	Reaction rate (mol s^{-1})
S_{cat}	Specific surface area of the Ag catalyst per electrode volume (m^2 m^{-3})
$S_{\text{domain,k}}$	Specific surface area of domain k per geometrical electrode area of the domain k (m^2 m^{-2})
$S_{\text{phase interface}}$	Specific surface area of the interface per geometrical electrode area (m^2 m^{-2})
T	Temperature (K)
v	Velocity (m s^{-1})
x_i	Mole fraction of species i (−)
z	Length (m)
$\|Z\|$	Impedance (Ω)
α	Charge transfer coefficient (−)
ε	Porosity (−)
γ_i	Activity coefficient of species i (−)
$\gamma_\pm$	Mean activity coefficient of NaOH (−)
η_{reaction}	Reaction overpotential (V)
μ_i	Chemical potential of species i (J mol^{-1})
ν_i^{ORR}	Stoichiometric coefficient of species i in ORR (−)
τ	Time constant (s)
τ	Tortuosity (−)

Sub- and superscripts

3PA	three-phase area
cat	Related to the catalyst surface
DL	Double layer
d	Distance from the liquid side of the ODC
eff	Effective
ext	External
F	Faradaic
fa	Flooded agglomerates
gas	Gaseous / gas phase
geo	Geometrical / related to the geometric ODC surface
int	Internal
i	Imaginary
k	Index of domain
l	Thickness of ODC
liq	Liquid / liquid phase
ldl	Liquid diffusion layer
R	Real
t	Total
tf	Thin-film
Θ	Standard state
∗	At gas-liquid interface

1 wt-% PTFE, respectively) and identified a silver content of 98 wt-% as best. The amount of silver had a very low influence on the polarization curve at low, e.g. kinetically governed current densities, but a significant influence on the performance at high current densities, i.e. in the mass transport dominated range of the polarization curve. It was hypothesized that the hydrophilic ODC with a high silver content of 99 wt-% was flooded by the liquid electrolyte, whereas ODC with a high PTFE content above 5 wt-% were too hydrophobic and electrolyte intrusion was insufficient. Both effects may lead to a decrease in the extent of the gas-liquid interface and thus to limitations due to oxygen availability. The authors pointed out that the electrolyte distribution is of upmost importance for understanding the ODC performance [8]. Paulisch et al. [9] investigated the electrolyte distribution in detail by operando X-ray radiography and chronoamperometric measurements. They showed that the pore structure as well as the distribution of the electrolyte during operations is inhomogeneous: some pores were barely flooded by the electrolyte, whereas a local breakthrough of the electrolyte to the oxygen side was observed in other pores [9]. The locally high electrolyte saturation seems surprising, as previous studies have shown that even very small amounts of PTFE lead to a non-wettability of a pore system [10]. In conclusion, the influences of PTFE content and local inhomogeneities on ODC performance are not fully understood yet, no models to quantitatively describe this influence are available. This hampers the knowledge-driven design of high performing electrodes. The importance of understanding inhomogeneities in liquid distribution in porous electrodes was already emphasized by various experimental and stimulative studies inter alia for proton-exchange membrane fuel cell (PEMFC) [11–13].

Methodically, dynamic simulations and experiments have been used successfully to discriminate processes by their time constants in many studies on various electrochemical systems [14,15]. This allows one e.g. to determine reaction kinetics [16] or to sense concentrations [17]. Model-based studies to investigate inhomogeneities were inter alia performed by Levi et al. who connected two different diffusion paths in parallel to study diffusion time constants for particle size distributions in non-uniform composite graphite electrodes for lithium-ion batteries [18] or by Jüttner and Lorenz who investigated the influence of surface inhomogeneities on corrosion processes for different metal electrodes in sodium hydroxide electrolyte [19]. Chevalier et al. interconnected single cell models to draw conclusions about the local distribution of the state-of-health of a PEMFC stack from the stack impedance spectra [20]. Krewer et al. have shown that local inhomogeneities in concentration in direct methanol fuel cells (DMFC) lead to characteristic changes of the dynamic behavior [21].

In this study, we present the first model for describing the influence of inhomogeneities in electrolyte distribution on ODC performance. Motivated by prior studies, dynamic model-based analysis is chosen as a tool because it offers a deeper insight. To this end, a previously published dynamic one-dimensional three-phase model of ODC [6] was extended to incorporate multiple electrode domains, each with different representative characteristics. The inhomogeneous ODC model is used to analyze experimental elec-

trochemical impedance spectra (EIS) as well as polarization curves of ODC with systematically varied silver catalyst content. We will show how to interpret the observed flattened semicircles in the impedance spectra regarding to local inhomogeneities. We demonstrate how the structure and silver content of ODC affect the electrolyte distribution, electrode performance and dynamics. The aim of this study is to infer the macroscopic distribution of the electrolyte from the performance and impedance spectra of the ODC. The methodology used does not allow conclusions to be drawn about microstructures such as pore size distribution or local electrolyte distributions. It will be discussed that not only the size of the gas-liquid interface but also the location is of importance for the performance. These are key findings to understand the influence of the electrode structure on the electrode performance and dynamics. EIS is shown to be a highly sensitive tool for diagnosing the electrolyte distribution within ODC.

2. Experimental

2.1. Electrode preparation

The preparation method and physical characterization for the examined electrodes is given in detail in a previous publication [8]. In short: For each electrode, we used a suspension containing silver particles (SF9ED, Ames Advanced Materials Corp., median of particle diameter: 2. 5 μm), [22] a methyl cellulose solution (1 wt-% WALOCEL^{TM} MKX 70000 PP 01) as pore building agent and thickener, demineralized water and a PTFE dispersion (TF 5060GZ, 3M^{TM} Dyneon^{TM}) in the desired ratio. The suspension was supplied with a spraying piston (Evolution, 0. 6mm pin hole, Harder & Steenbeck) on a conductive support (nickel mesh, 106 μm x 118 μm mesh size, 63 μm thickness, Haver & Boecker OHG) with a total of 80 layers. In the further production steps the electrodes were hot pressed (LaboPress P200S, Vogt, 15 MPa, 130 °C, 5 min) and sintered in an air oven (330 °C, 15 min) to improve the mechanical stability and to form the pore system by burning out the methyl cellulose completely. Detailed characteristics of the ODC, such as catalyst loading or electrode density, are also given in a previous publication [8].

2.2. Electrochemical characterization

Electrochemical experiments were performed using a half-cell set up (FlexCell HZ PP01, Gaskatel GmbH) with a geometrical cell area of 3.14 cm^2 in a three electrode configuration. A platinum wire acts as a counter electrode while the potentials were measured with a reversible hydrogen electrode (RHE) through a Luggin capillary in front of the GDE.

The half-cell consists of an electrolyte and gas compartment divided by the GDE. As electrolyte approximately 30 mL of a 30 wt-% NaOH solution was prepared from caustic flakes ($\leq$ 99 wt-%, Carl Roth) and demineralized water. In the gas compartment pure oxygen with a flowrate of 50 mLN min^{-1} and a small back pressure using a 1mm water column was applied. The whole half-cell was heated up to 80 °C to correspond to industrial conditions [4]. The experiments were carried out with a Zennium Pro Potentiostat (Zahner GmbH) following the same routine for each electrode. In a startup procedure current densities of 1, 2, 3 and 4 kA m^{-2} were applied for conditioning the electrodes. Afterwards pseudo-galvanostatic impedance measurements were performed at current densities of 2 kA m^{-2}. A 10 mV amplitude was applied using a single sine with a starting frequency of 1 Hz going up to the upper limit of 50 kHz and sweeping down to the lower limit of 100 mHz. Sampling the frequencies between in the high frequency range twice is a standard proceed to stabilize the measurement. Afterwards linear sweep voltammetry (LSV) starting at open cell potential (OCP) to 200 mV vs. reversible hydrogen electrode (RHE) with a scan rate of 0.5 mV s^{-1} was performed to obtain the polarization curves.

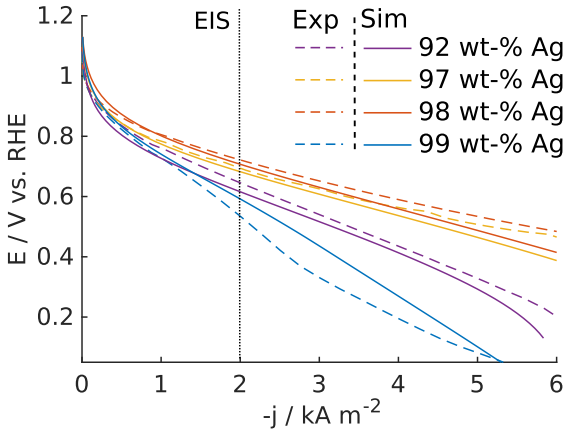

Fig. 1. Experimental [8] and simulated polarization curves of ODC with different Ag-content.

3. Measurement results

In this section, the measurement results which will be used for validating the simulations are explained and interpreted. As discussed in detail by Franzen et al., the Ag ratio of the ODC has a major effect on the stationary performance of ODC [8]. Thus, the polarization curves of four ODC with distinct silver-PTFE ratio have been chosen for further analysis from previously published data [8]:

- **92 wt-% Ag**: This composition exhibits a medium performance and hydrophobic properties. (Electrode thickness: 292 μm) [8]
- **97 wt-% Ag**: The structure of an ODC with 97 wt-% Ag has been analysed by Neumann et al. [23], so that identified structure parameter can be used in this study. (Electrode thickness: 297 μm [8])
- **98 wt-% Ag**: This composition exhibits the best performance [8]. (Electrode thickness: 335 μm)
- **99 wt-% Ag**: This composition exhibits a low performance and hydrophilic properties [8] (Electrode thickness: 356 μm).

In the following, the ODC are denoted by their silver content; the PTFE content is equal to rest of the mass fraction. The polarization curves of these ODC are given in Fig. 1. The main differences between the electrodes occur at current densities above 2000 A m^{-2}. To explore the reasons of the different performances, electrochemical impedance measurements are conducted in this study, the results of which are given in Fig. 2a). All impedance spectra show distorted semi-circles. For the ODC with 99 wt-%, a second semicircle emerges at high frequencies. The ODC mainly differ in terms of ohmic and charge transfer resistance. The ohmic and the charge transfer resistance R_{CT} of the different impedance spectra is determined as [24]:

$$R_{CT} = Z_R(f_{min}) - Z_R(f_{max}) \quad (2)$$

With Z_R as the real part of the impedance Z and f as the frequency, where $Z_R(f_{max})$ is the ohmic resistance. There is no systematic correlation between ohmic resistance and silver content or performance of ODC; the differences result from slightly different distances between the ODC and the reference electrode, since sealing elements are tightened by hand and therefore their compres-

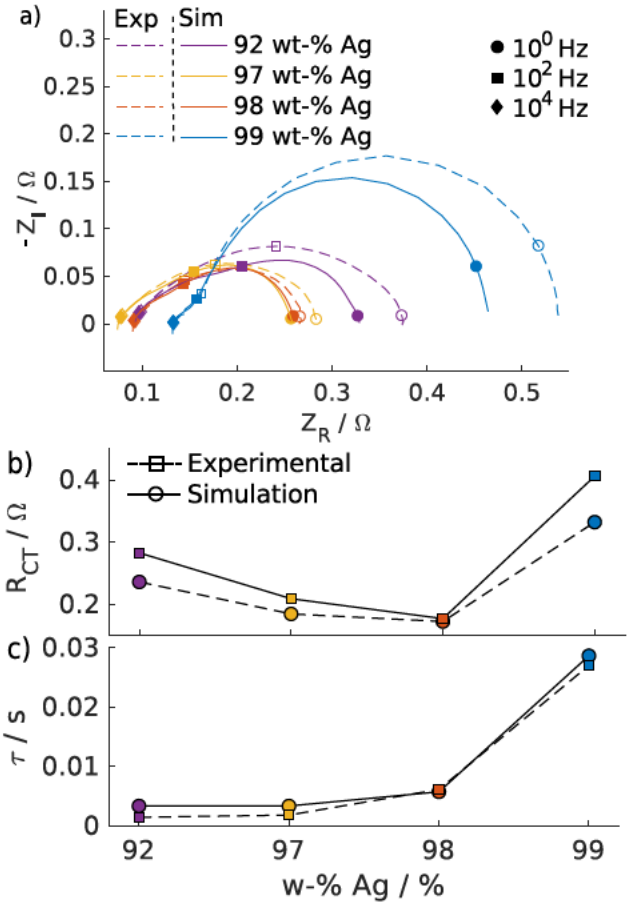

Fig. 2. a) Simulated and experimental EIS at $j = 2000$ A m^{-2} of ODC with different Ag-content, b) calculated charge transfer resistance and c) calculated time constants from experimental and simulated EIS.

sions differ. The resulting values for R_{CT} are shown in Fig. 2b). The smallest charge transfer resistance is obtained for the ODC with 98 wt-% Ag, the largest for 99 wt-% Ag, which agrees with the performance ranking in stationary measurements. To identify the associated processes, the time constants were determined from the impedance data by Eq. (3):

$$\tau = \frac{1}{2\pi f(-Z_{I,max})} \tag{3}$$

$f(-Z_{I,max})$ is the frequency where the negative imaginary part of the impedance reaches its maximum. The results are given in Fig. 2c). Two trends are visible: First, the time constant is increasing with an increasing Ag-content, but does not correlate with ODC performance. Second, for all four ODC the characteristic time constant is in the range of 0.0015 s to 0.03 s, which agrees with our previous results from potential step measurements [25]. It should be noted that the potential step measurements cover a larger range of time constants than EIS [16], and that no time constants slower than those found here were observed [25]. The charge transfer resistance reaches a minimum at 98 wt-% Ag, but the time constant decreases further until 92 wt-% Ag.

In principle, the measured semi-circle and the corresponding time constants can be caused by transport processes, by the interplay of reaction and double layer charging, or a combination of both. However, mass transport can be excluded in this case. The time constant of a diffusion process τ_{mt} for species i in j can be approximated from Fick's second law [14]. Equation (4) gives the diffusion time constant within a porous media, which is proportional to the square of the characteristic diffusion length, i.e. the electrode thickness Δz, the porosity ε and inversely proportional to the binary diffusion coefficient $D_{i,j}^{eff}$ of species i in j.

$$\tau_{mt} \approx \frac{\Delta z^2}{D_{i,j}^{eff}} \cdot \varepsilon \tag{4}$$

We analysed the diffusion processes in ODC in a previous publication. We demonstrated that a long mass transport way in the liquid phase leads to a distinct time constant in chronoamperometric measurements due to the water and hydroxide ion mass transport, whereas no distinct time constants for oxygen transport – in the gas as well as in the liquid phase – were found [25]. For *j* as water and *i* as NaOH, a flooding degree of the ODC from 5 % to 50 % with $D_{i,j}^{eff} = 3.20 \times 10^{-10}$ m^2 s^{-1} (cf. Table 5) and $\varepsilon = 0.4$ would lead to time constants of 0.28 to 28.2 s, which is orders of magnitudes higher than the measurement results. Also, the results in Fig. 2 suggest that the observed time constant is not determined by oxygen transport in the gas phase, since the time constants become faster with increasing hydrophilicity and thus decreasing mass transport length in the gas phase. Although the current density of ODC is limited by the availability of dissolved oxygen in the liquid electrolyte [6,25,26], oxygen transport in the liquid phase can also be excluded as the process causing the measured semi-circles for two reasons: First, as shown before, the diffusion length of the oxygen in the liquid phase is only several tens nanometers [26,27] up to a few hundred nanometers [28], and the associated time constant is smaller than 10×10^{-6} s [6]. This is orders of magnitudes faster than the time constants measured here. Second, the time constants of all ODC differ while oxygen diffusivity in the electrolyte is not expected to be changed with the electrolyte distribution or electrode composition.

In shutdown measurements with comparable ODC, double layer capacitances of about $C_{dl} = 50$ F m^{-2} were identified [29]. The time constant of the double layer charge / discharge taking place in parallel to a faradaic reaction is given by Eq. (5) [24]:

$$\tau_{dl} = C_{dl} \cdot A_{geo} \cdot R_{CT} \tag{5}$$

With the characteristic time constant τ_{dl}, the double layer capacitance per geometrical area C_{dl}, and the geometrical electrode area A_{geo}. Using $C_{dl} = 50$ F m^{-2}, $R_{CT} = 0.2$ Ω and $A_{geo} = 6.28 \times 10^{-5}$ m^2 (cf. Fig. 2b), $\tau_{dl} = 0.003$ s is obtained, which is in the range of the measured time constants (cf. Fig. 2c). This hypothesis is also supported by the fact that the measured time constants correlate with the silver content – which increases the available surface area and thus the double layer capacitance and decreases the time constant – and not with the ODC performance.

In conclusion, the semi-circles of the EIS measurement represent only the double layer charge and discharge and no mass transfer. In this context, the distorted shape of the semi-circles is surprising because the interplay of double layer capacitance and a single reaction in a homogeneous electrode would lead to a non-distorted semicircle. Although two parallel reactions pathways for the alkaline ORR are known, both have the same rate determining step [30]. Thus, no influences on the dynamics of complex kinetic processes at the electrode surface are expected and the distortion of the semi-circles is most likely not caused by two overlaying reaction processes. The distortion of the semi-circles could, however, be caused by inhomogeneous electrode properties. As studied by Lukács, a distribution of process parameters within an electrochemical system leads to detached semi-circles [31]. Paulisch et al. measured an inhomogeneous electrolyte distribution in the ODC [9]. Based on these studies, we assume that the distorted semi-circles of the ODC impedances reflect locally different reaction rates and double layer capacitances due to inhomogeneities of the electrolyte distribution. Gradients in the local reaction rates have

Table 1
Model equations.

Electrode charge and reaction

Faraday current

$$j_F(t) = -F \cdot 4 \cdot \int_{z_l - z_{fa}}^{z_l} r(z,t)\mathrm{d}z \tag{6}$$

Reaction rate [34]

$$r(z) = k_{0,cat} \cdot S_{cat} \cdot a_{O_2}(z,t) \cdot \exp\left(-\frac{(1-\alpha)\cdot F \cdot \eta_{reaction}(z,t)}{R \cdot T}\right) \tag{7}$$

Reaction overpotential

$$\eta_{reaction}(z,t) = E_{int}(t) - E_0(z,t) \tag{8}$$

Nernst potential [34]

$$E_0(z,t) = E_{00} + \frac{R \cdot T}{4 \cdot F} \ln\left(\frac{a_{O_2}(z,t) \cdot a_{H_2O}^2(z,t)}{a_{NaOH}^4(z,t)}\right) \tag{9}$$

Activity of O_2

$$a_{O_2}(z,t) = x_{O_2}(z,t) \cdot \gamma_{O_2}(z,t) \tag{10}$$

Activity of NaOH

$$a_{NaOH}(z,t) = \frac{b_{NaOH}(z,t)}{b_{NaOH}^{\ominus}} \cdot \gamma_{\pm}(z,t) \tag{11}$$

Molality of NaOH

$$b_{NaOH}(z,t) = \frac{n_{NaOH}(z,t)}{m_{electrolyte}(z,t)} \tag{12}$$

Ohmic drop

$$E_{ext}(t) - E_{int}(t) = R_{specific} \cdot j(t) \tag{13}$$

Charge balance

$$\int_{z_l - z_{fa}}^{z_l} c_{dl,cat} \cdot S_{cat}\ \mathrm{d}z\ \frac{\mathrm{d}E_{int}(t)}{\mathrm{d}t} = j(t) - F \cdot 4 \cdot \int_{z_l - z_{fa}}^{z_l} r(z,t)\mathrm{d}z \tag{14}$$

Mass transport in the gas phase and processes at the gas-liquid interface

Species balance

$$\frac{\partial p_i(z,t)}{\partial t} \cdot \varepsilon = \frac{\partial^2 p_i(z,t)}{\partial z^2} \cdot \mathscr{D}_{i,j}^{gas,eff} + \frac{\partial p_i(z,t)}{\partial z} \cdot v_{gas}(t) \tag{15}$$

with $i = \{H_2O, O_2\}$

Effective diffusion coefficient

$$\mathscr{D}_{i,j}^{gas,eff} = \mathscr{D}_{i,j}^{gas} \cdot \frac{\varepsilon}{\tau} \tag{16}$$

Bruggemann correlation

$$\tau = \varepsilon^{-0.5} \tag{17}$$

Henry's law

$$c_{O_2}^*(t) = \frac{p_{O_2}^*(t)}{H_{O_2}(c_{NaOH}^*(t), c_{H_2O}^*(t))} \tag{18}$$

Stefan flow

$$\frac{p_{total}}{R \cdot T} \cdot v_{gas}(t) = \dot{N}_{H_2O}^{evaporation}(t) - \dot{N}_{O_2}^{dissolution}(t) \tag{19}$$

Specific surface area of phase interface

$$S_{phase\ \ interface} = \frac{A_{phase\ \ interface}}{A_{domain}} \tag{20}$$

(*continued on next page*)

Table 1 (*continued*)

Mass transport in the thin film

Species balance

$$\frac{dc_i(z,t)}{dt} = \sum_{\substack{j=1 \\ i\neq j}}^{n} \frac{Đ_{i,j}}{RT}\left(\left(\frac{\partial^2\mu_i(z,t)}{\partial z^2} - \frac{\partial^2\mu_j(z,t)}{\partial z^2}\right)\cdot\frac{c_i(z,t)c_j(z,t)}{c_{\text{total}}}\right. \tag{21}$$

$$+\left(\frac{\partial\mu_i(z,t)}{\partial z} - \frac{\partial\mu_j(z,t)}{\partial z}\right)\cdot\frac{\partial c_i(z,t)}{\partial z}\frac{c_j(z,t)}{c_{\text{total}}} + \left(\frac{\partial\mu_i(z,t)}{\partial z} - \frac{\partial\mu_j(z,t)}{\partial z}\right)\cdot\frac{\partial c_j(z,t)}{\partial z}\frac{c_i(z,t)}{c_{\text{total}}}\Bigg) \tag{22}$$

$$+\frac{\partial c_i(z,t)}{\partial z}\cdot v_{\text{liq,evaporation}}(t) \tag{23}$$

with $i = \{OH^-, H_2O, O_2\}$, $j = \{OH^-, H_2O\}$

Chemical potential of NaOH [26]

$$\mu_{\text{NaOH}}(z,t) = \mu_{Na^+}(z,t) + \mu_{OH^-}(z,t) = \mu^{\ominus}_{\text{NaOH}} + RT\ln\left(\gamma^2_{\pm}(z,t)\left(\frac{b_{\text{NaOH}}(z,t)}{b^{\ominus}_{\text{NaOH}}}\right)^2\right) \tag{24}$$

Chemical potential of H_2O and O_2

$$\mu_i(z,t) = \mu_i^{\ominus}(z,t) + RT\cdot\ln\left(a_i(z,t)\right) \tag{25}$$

with $i = \{O_2, H_2O\}$

Maxwell-Stefan Diffusity [37]

$$Đ_{O_2,j}(z,t) = \mathscr{D}_{O_2,j}\frac{\partial\ln\left(x_{O_2}(z,t)\right)}{\partial\ln\left(a_{O_2}(z,t)\right)} \tag{26}$$

with $j = \{OH^-, H_2O\}$

Velocity due to evaporation

$$v_{\text{liq,evaporation}}(t) = \frac{\dot{N}^{\text{gas,in}}_{H_2O}(t)}{c^{*}_{H_2O}(t)} \tag{27}$$

Mass transport in the flooded agglomerates

Species balance

$$\frac{dc_i(z,t)}{dt}\cdot\varepsilon = \sum_{\substack{j=1 \\ i\neq j}}^{n} \frac{Đ^{\text{liq,eff}}_{i,j}}{RT}\left(\left(\frac{\partial^2\mu_i(z,t)}{\partial z^2} - \frac{\partial^2\mu_j(z,t)}{\partial z^2}\right)\cdot\frac{c_i(z,t)c_j(z,t)}{c_{\text{total}}}\right. \tag{28}$$

$$+\left(\frac{\partial\mu_i(z,t)}{\partial z} - \frac{\partial\mu_j(z,t)}{\partial z}\right)\cdot\frac{\partial c_i(z,t)}{\partial z}\frac{c_j(z,t)}{c_{\text{total}}} + \left(\frac{\partial\mu_i(z,t)}{\partial z} - \frac{\partial\mu_j(z,t)}{\partial z}\right)\cdot\frac{\partial c_j(z,t)}{\partial z}\frac{c_i(z,t)}{c_{\text{total}}}\Bigg) \tag{29}$$

$$+\frac{\partial c_i(z,t)}{\partial z}\cdot v_{\text{liq}}(z,t) - r(z,t) \tag{30}$$

with $i = \{OH^-, H_2O, O_2\}$, $j = \{OH^-, H_2O\}$

Velocity due to reaction

$$v_{\text{liq,react}}(z,t) = (|\nu^{\text{ORR}}_{H_2O}| - |\nu^{\text{ORR}}_{OH^-}|)\int_{z_l - z_{fa}}^{z_l}\frac{r(z,t)}{c_{\text{total}}}dz \tag{31}$$

Total velocity

$$v_{\text{liq}}(z,t) = v_{\text{liq,evaporation}}(t) + v_{\text{liq,react}}(z,t) \tag{32}$$

Mass transport in the liquid diffusion layer

Species balance

$$\frac{dc_i(z,t)}{dt}\cdot\varepsilon = \sum_{\substack{j=1 \\ i\neq j}}^{n} \frac{Đ^{\text{liq,eff}}_{i,j}}{RT}\left(\left(\frac{\partial^2\mu_i(z,t)}{\partial z^2} - \frac{\partial^2\mu_j(z,t)}{\partial z^2}\right)\cdot\frac{c_i(z,t)c_j(z,t)}{c_{\text{total}}}\right. \tag{33}$$

$$+\left(\frac{\partial\mu_i(z,t)}{\partial z} - \frac{\partial\mu_j(z,t)}{\partial z}\right)\cdot\frac{\partial c_i(z,t)}{\partial z}\frac{c_j(z,t)}{c_{\text{total}}} + \left(\frac{\partial\mu_i(z,t)}{\partial z} - \frac{\partial\mu_j(z,t)}{\partial z}\right)\cdot\frac{\partial c_j(z,t)}{\partial z}\frac{c_i(z,t)}{c_{\text{total}}}\Bigg) \tag{34}$$

$$+\frac{\partial c_i(z,t)}{\partial z}\cdot v_{\text{ldl}}(t) \tag{35}$$

with $i = \{OH^-, H_2O, O_2\}$, $j = \{OH^-, H_2O\}$

Interconnection of the ODC domains

Specific domain area

$$S_{\text{domain,k}} = \frac{A_{\text{domain,k}}}{A_{\text{geo}}} \tag{36}$$

(*continued on next page*)

Table 1 (*continued*)

Molar flow density out of / into liquid diffusion layer	$\dot{N}^{\mathrm{ldl}}(t) = \sum_{k=1}^{n=5} \dot{N}_{i,k}^{\mathrm{fa}}(t) \cdot S_{\mathrm{domain,k}}$	(37)
Molar flow density out of / into flooded agglomerates	$\dot{N}_i^{\mathrm{fa}}(t) = -\sum_{\substack{j=1 \\ i \neq j}}^{n} \left(\frac{Đ_{i,j}}{RT} \frac{c_i(z,t) c_j(z,t)}{c_{\mathrm{total}}} \left(\frac{\partial \mu_i(z,t)}{\partial z} - \frac{\partial \mu_j(z,t)}{\partial z} \right) + c_i(z,t) \cdot \nu_{\mathrm{liq,k}}(z,t) \right) \Big\|_{z=z_{\mathrm{l}}}$	(38)
Local velocity	$\nu_{\mathrm{ldl}}(t) = \sum_{k=1}^{n=5} S_{\mathrm{domain,k}} \cdot \nu_{\mathrm{liq,k}}(z = z_{\mathrm{l}}, t)$	(39)
Total current density	$j_{\mathrm{ODC}}(t) = \sum_{k=1}^{n=5} j_{\mathrm{domain,k}}(t) \cdot S_{\mathrm{domain,k}}$	(40)
Boundary conditions		
O_2 in gas bulk	$p_{O_2}(z = 0) = p_{\mathrm{total}}$	(41)
H_2O in gas bulk	$p_{H_2O}(z = 0) = 0$	(42)
O_2 in electrolyte bulk	$c_{O_2}(z = z_{\mathrm{t}}) = 0$	(43)
NaOH in electrolyte bulk	$c_{\mathrm{NaOH}}(z = z_{\mathrm{t}}) = c_{\mathrm{NaOH}}(z = z_{\mathrm{t}}, t = 0)$	(44)
H_2O in electrolyte bulk[a]	$c_{H_2O}(z = z_{\mathrm{t}}) = f(c_{\mathrm{NaOH}}(z = z_{\mathrm{t}}, t = 0))$	(45)
Electrode geometry	$z_{\mathrm{gas}} + z_{\mathrm{tf}} + z_{\mathrm{fa}} = z_{\mathrm{l}}$	(46)

[a] Calculated as in [38]

inter alia already been reported for DMFC anodes and cathodes [32], or for acid ORR in PEMFC cathodes [33]. Based on this analysis of the experimental data, we employ a dynamic three-phase model which encompasses the effects of local inhomogeneities on the electrode to further analyze the processes in an ODC.

4. Modelling

It is known, that the electrodes are inhomogeneous in particle size, pore size distribution as well as in the local catalyst and binder loading [23]. These local inhomogeneities in turn lead to a distribution of hydrophilic and hydrophobic properties of the different pores [10] and may explain the previously observed electrolyte distribution [9]. The processes in the inhomogeneous three-dimensional GDE are very complex and include the effects of microkinetics [34], electrowetting [9] or closed pores [8]. Thus it is necessary to simplify the structure and processes in macroscopic model approach to describe electrode performance. The presented model focuses on the effect of an inhomogeneous electrolyte distribution and three-phase area on electrode performance. Determining an electrolyte distribution from the electrode microstructure would require a detailed understanding of factors such as pore size distributions, local surface properties inside the pores or local tortuosity, but also two-phase flow in porous media, and is out of scope of this work. The electrolyte distribution is particularly important because it governs the mass transfer paths for the water and the hydroxide ions in the liquid phase, the oxygen dissolution via the size and location of the gas-liquid interface and the area for reaction and double layer charge/discharge via the size of the wetted catalyst surface per volume.

The model of an inhomogeneous ODC is developed by dividing the ODC in multiple domains perpendicular to the through-plane coordinate z. The domains are connected in parallel and differ in the penetration depth of the electrolyte and the size of the gas-liquid interface, as shown in Fig. 3a). Each domain submodel is discretised in through-plane direction (z), see Fig. 3b). This model is based on the assumption that the preferred mass transport is along the z coordinate in the through-plane direction, between the gas and the liquid bulk. Since the mass transport ways in in-plane direction are comparatively long (electrode thickness: 0.3 mm thick; electrode diameter: 20 mm) and run parallel to the two bulk phases, mass transport in in-plane direction

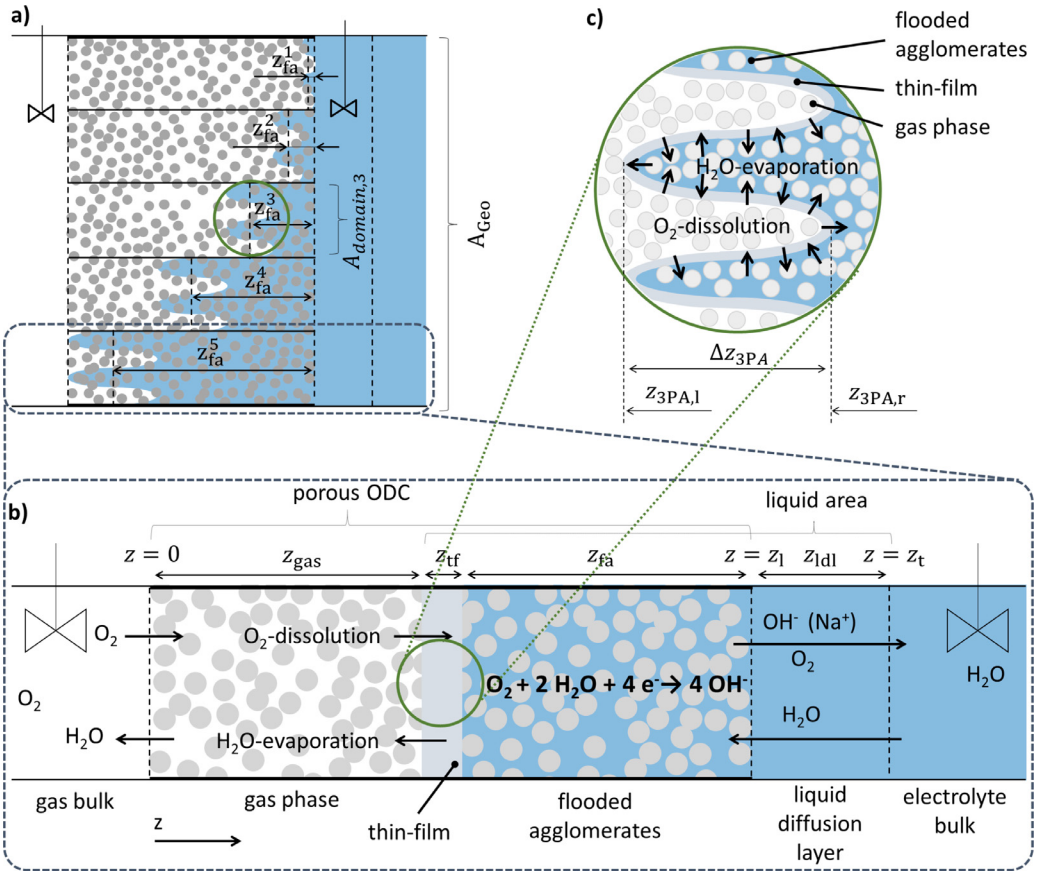

Fig. 3. a) Schematic view of the model of an inhomogeneous ODC comprised of multiple homogeneous sub-domains, b) Schematic view of the domain sub-model including reaction and mass transport, c) zoom at the gas-liquid interface.

is assumed to be negligible. The aim of the model is to demonstrate how the inhomogeneity influences the performance and the dynamics of the ODC. The used approach does not allow one to replicate electrode structures in all aspects, but to derive important conclusions about the impact of the inhomogeneous electrolyte distribution.

In the following, first the domain sub-model is explained. Subsequently, the interconnection of the domain sub-models to an inhomogeneous ODC is outlined. Model equations are given in Table 1.

4.1. The domain sub-model

The domain sub-model is adapted from our previously introduced model of an ODC with a homogeneous structure [6]. Herein the domain sub-model is shortly summarized, a detailed description including all model assumptions is given in the corresponding publication mentioned above.

The dynamic one-dimensional three-phase thin-film model of a homogeneous ODC, is divided into four sections in in-plane (z-) direction. Three of them are located within the ODC, a gas phase, a liquid phase and a thin-film (cf. Fig. 3b)): The oxygen enters the electrode through the gas phase and the evaporated water leaves through it. The flooded agglomerates resemble the flooded part of the GDE where reaction and liquid transport take place. The thin-film is the interphase between the gas and the liquid phase, where species change from liquid to gaseous state and vice versa.

The Faradaic current density $j_F(t)$ of the ORR is modeled by Faraday's law Eq. (6) and the Tafel Eq. (7). Complete ORR (eq. 1) is assumed, where the rate determining step is the formation of the superoxide radical anion under the acceptance of one electron [34,35]. This mechanism is valid in ODC for reaction overpotentials ≥ 0.155 V [26]. The reaction overpotential of the ORR is calculated as the difference between potential in the reaction zone $E_{int}(t)$ and the open circuit potential $E_0(z,t)$ Eq. (8), which is calculated by the Nernst equation (9). Hereby, the internal potential $E_{int}(t)$ is calculated by subtracting the ohmic drop Eq. (13) from the measured external potential E_{ext}. Finally, the charge balance Eq. (14) contains the charge storage by internal potential, double layer capacitance C_{dl} and the production or consumption of charge by reaction.

The mass transport in the gas phase across the porous electrode is described by the bilateral non-equimolar diffusion Eq. (15) [36], which includes, besides Fick's diffusion, also the convective Stefan flow as a result of water evaporation Eq. (19) and oxygen dissolution Eq. (18) at the gas-liquid interface. For Stefan flow, constant pressure p_{total} and therefore a constant local velocity is assumed. The velocity is obtained from the difference between the fluxes of oxygen dissolution and water evaporation. The specific surface of the gas-liquid interface for each domain is modeled by Eq. (20) (cf. Fig. 3c).

The multi-component mass transport in the thin-film is modeled by Maxwell-Stefan diffusion with overlaying convection due to evaporation Eq. (23). In contrast to our previous publications [6,25], the Maxwell-Stefan diffusion is modeled to be not concentration, but chemical potential driven. The chemical potential of NaOH is calculated respecting the law of electroneutrality using the mean activity coefficient $\gamma_{\pm}(z,t)$, Eq. (24) [26]. Fick's diffusion coefficient of oxygen is adapted by an approach given by Bird and Klingenberg [37], Eq. (26). The velocity of the convective flow is

assumed to be constant over the length of the thin-film and calculated by Eq. (27).

The mass transport within the flooded agglomerates is described by Maxwell-Stefan diffusion with overlaying convective Stefan flow Eq. (30). The velocity of the convective flow $v_{\mathrm{liq}}(z,t)$ consists of two components, one due to evaporation $v_{\mathrm{liq,evaporation}}(t)$ and one due to the change in density of the liquid electrolyte caused by the reaction rate dependent enrichment of ions $v_{\mathrm{liq,react}}(z,t)$, Eq. (31).

The mass transport in the liquid diffusion layer is similar to the mass transport in the flooded agglomerates, but assuming free diffusion. The convective velocity within the liquid diffusion layer does not change over the location. The calculation of the convective velocity is discussed in detail in next section with regard to the model of an inhomogeneous ODC. The boundary conditions are given in Eq. (41)–(45).

4.2. The inhomogeneous ODC Model

This model connects the single sub-domain models to an inhomogeneously flooded ODC model. Each domain k takes up a specified proportion $S_{\mathrm{domain,k}}$ of the total geometrical electrode area A_{geo} (Eq. (36)). The domains are separated in through-plane direction, but connected by a common liquid diffusion layer (cf. Fig. 3a)). The concentrations c_i at the boundary between the flooded agglomerates and the liquid diffusion layer are obtained by solving Eq. (37). Accordingly, the velocity of the convective flow in liquid diffusion layer is calculated by Eq. (39). Since it has been shown that oxygen transport in the gas phase does not significantly affect the dynamics and performance of the ODC [6], it was decided not to interconnect the mass transport in the gas phase to simulate the inhomogeneities. Electrically, the domains are connected in parallel circuit, so that the total current density of the cathode equals the sum of all cathode domains, weighted by their share of the total area, Eq. (40).

4.3. Properties and parameters of ODC and representative electrode domains

In this section, the properties of the different ODC and their representative domains are discussed. The model parameters are classified on three levels:

1. Parameters that are assumed to be identical for all ODC and to have no distribution in the ODC: The catalyst surface area specific reaction rate constant $k_{0,\mathrm{cat}}$ and the catalyst surface area specific double layer capacitance $C_{\mathrm{dl,cat}}$.
2. Parameters that are assumed to be constant for each ODC, but differ between the individual ODC: The ohmic resistance R_{specific}, the porosity ε and the specific surface area of the catalyst S_{cat}.
3. Parameters that are assumed to be distributed within the ODC: The intrusion length z_{fa} of the electrolyte and the local size of the gas-liquid interface $S_{\mathrm{phase\ interface}}$ as well as relative size of the domains $S_{\mathrm{domain,k}}$.

As it is clear that properties are distributed and that the goal of the study is to identify a distribution that can reproduce the experiments via numerical parameterization, we limit the number of simulated domains to five. This number allows to have flooded, empty and several differently flooded pores; areas with similar flooding degrees are lumped together, as the domains do only interact via the joint bulk phases. Since some parameters are independent while other parameters are connected through physical interrelationships to others, their (in)dependencies are discussed in the following.

Table 2
Geometrical dimensions of the three-phase area of the different domains.

Domain -	$z_{\mathrm{3PA,l}}$[a] μm	$z_{\mathrm{3PA,r}}$ μm	z_{fa} μm	Δz_{3PA} μm
1	$0.01 \cdot z_{\mathrm{l}}$	$0 \cdot z_{\mathrm{l}}$	$0.005 \cdot z_{\mathrm{l}}$	$0.01 \cdot z_{\mathrm{l}}$
2	$0.032 \cdot z_{\mathrm{l}}$	$0.01 \cdot z_{\mathrm{l}}$	$0.022 \cdot z_{\mathrm{l}}$	$0.022 \cdot z_{\mathrm{l}}$
3	$0.1 \cdot z_{\mathrm{l}}$	$0.032 \cdot z_{\mathrm{l}}$	$0.066 \cdot z_{\mathrm{l}}$	$0.068 \cdot z_{\mathrm{l}}$
4	$0.316 \cdot z_{\mathrm{l}}$	$0.1 \cdot z_{\mathrm{l}}$	$0.208 \cdot z_{\mathrm{l}}$	$0.216 \cdot z_{\mathrm{l}}$
5	$1.0 \cdot z_{\mathrm{l}}$	$0.316 \cdot z_{\mathrm{l}}$	$0.658 \cdot z_{\mathrm{l}}$	$0.684 \cdot z_{\mathrm{l}}$

[a] Logarithmic scale from 0.01 to 1.

First, we fixed an electrolyte distribution that covers a three-phase zone which extends across the entire ODC. For this purpose, the flooding length of the different domains z_{fa}, as well as the length of the three-phase areas Δz_{3PA} – calculated by their left $z_{\mathrm{3PA,l}}$ and right boundaries $z_{\mathrm{3PA,r}}$ – are considered: As illustrated in (cf. Fig. 3c) the maximum intrusion depth of the electrolyte in each representative electrode domain marks the left side boundary of the three-phase area $z_{\mathrm{3PA,l}}$. We assume that some pores are blocked by hydrophobic PTFE at the beginning of the electrode, while other pores are completely flooded. Thus the maximium intrusion depth of the electrolyte is assumed to be in the rang between 1 % up to 100 % of the electrode thickness. A logarithmic scale was chosen since it is expected that due to the high hydrophobicity of PTFE many pores are impermeable to the liquid electrolyte, leaving a large part of the electrode area with almost no electrolyte intrusion. In Table 2, the values of $z_{\mathrm{3PA,l}}$ for the five representative electrode domains are shown. The flooding degree increases monotonically from domain 1 (minimum flooding) to domain 5 (maximum flooding). A second assumption is that the three-phase area of the full electrode extends over the entire electrode thickness, but is split between the domains: For the more flooded domains, it is located closer to the gas bulk, and for the least flooded parts it is located close to the liquid diffusion layer. The right side boundary of the three-phase area $z_{\mathrm{3PA,r}}$ of one domain equals the left side boundary of the next less flooded domain so that there are no overlaps or gaps in the three-phase area. The thickness of the three-phase area is calculated by $\Delta z_{\mathrm{3PA}} = z_{\mathrm{3PA,l}} - z_{\mathrm{3PA,r}}$. The mean length of the flooded agglomerates of a domain z_{fa} is the mean value of the left side and the right side boundary of the three-phase area of the domain (cf. 3 a), more detailed in Fig. 1 and Fig. 2 in [6]). The oxygen gradient within the liquid electrolyte is very steep, [26,39], thus almost no ORR outside of the three-phase area takes place, especially at higher current densities [6]. The resulting values for $z_{\mathrm{3PA,l}}$, $z_{\mathrm{3PA,r}}$ and z_{fa} are given in Table 2.

Next the dependency of the local reaction rate (cf. Eq. (7)) as well as the double layer capacitance (cf. Eq. (14)) on the catalytically active Ag surface S_{cat} area are discussed. It can be assumed that the surface area specific reaction rate constant $k_{0,\mathrm{cat}}$ as well as the surface area specific double layer capacitance $C_{\mathrm{dl,cat}}$ are constant material properties. Thus differences in total catalytic activity and double layer capacitance between the different ODC only result from differences in electrode design, and thus in the specific catalyst surface area S_{cat} and in the wetted share of the catalyst. Neumann et al. obtained a specific surface area of $S_{\mathrm{cat}} = 6 \times 10^5\ \mathrm{m^2\ m^{-3}}$ Ag catalyst per electrode volume for ODC with 97 wt-% Ag [23]. Taking these values into account, Eqs. (7) and (14) can be used to identify $k_{0,\mathrm{cat}}$ and $C_{\mathrm{dl,cat}}$ from the measurements of ODC with 97 wt-%. The values for $k_{0,\mathrm{cat}}$ and $C_{\mathrm{dl,cat}}$ are used for all investigated ODC, and only the specific catalyst surface area is adjusted for each electrode. As shown before, the double layer capacitance depends on the current density [29], therefore, the value of $C_{\mathrm{dl,cat}}$ determined here is only valid for current densities of $j = 2000\ \mathrm{A\ m^{-2}}$.

Table 3
Parameters identified from (electrochemical) experiments and ODC model for electrodes with different Ag content as well as literature data.

Name	Symbol	Unit	99 wt-%	98 wt-%	97 wt-%	92 wt-%
Reaction rate constant	$k_{0,cat}$	mol $m^{-2}s^{-1}$			0.39	
Double layer capacitance	$C_{dl,cat}$	F m^{-2}			1.22	
Porosity	ε	–	0.4	0.37	0.355[a]	0.26
Specific catalyst interface	S_{cat}	$\mu m^2 \mu m^{-3}$	0.92	0.79	0.6[a]	0.58
Specific resistance[b]	$R_{specific}$	Ωm^2	4.15×10^{-5}	2.83×10^{-5}	2.32×10^{-5}	2.82×10^{-5}

[a] Determined by Neumann et al. [23]. [b] High frequency resistance from EIS measurements.

Table 4
Distributed parameters identified from electrochemical experiments and ODC model for electrodes with different Ag content.

Name	Symbol	Unit	Domain	99 wt-%	98 wt-%	97 wt-%	92 wt-%
Specific domain area	S_{domain}	%	1	3.20	5.19	12.1	22.0
			2	10.4	16.86	16.9	22.0
			3	24.0	37.74	38.6	35.2
			4	18.4	22.05	19.3	12.3
			5	44.0	18.16	13.3	8.5
Specific gas- liquid interface per thickness of three-phase-area	$\frac{S_{phase\ interface}}{\Delta z_{3PA}}$	$\mu m^2 \mu m^{-3}$	1	2.94	4.48	3.54	2.68
			2	8.71	9.89	7.65	6.02
			3	4.30	6.55	3.44	1.9
			4	0.08	0.15	0.11	0.05
			5	0.02	0.03	0.02	0.01

Within ODC the porosity ε may be distributed. Future work might elucidate how the local porosity is related to the silver/PTFE distribution and the electrolyte intrusion. Since this complex relationship is not clear yet, we use the simplifying assumption of equally distributed porosities, so that average porosity ε is set to be constant for all domains of a given electrode. The porosity, however, is dependent on the electrode design and electrode structure. It has been calculated to be 0.355 for the ODC with 97 wt-% Ag [23] and is adjusted for all further investigated electrodes and domains to reproduce the measurements.

The area-specific internal resistance of the different electrodes $R_{specific}$ was calculated from the impedance at the intersection with the real axis at high frequencies. The electric conductivity of the ODC is assumed to be high due to the high amount of Ag [26]; thus, variations in electric conductivity can be neglected and $R_{specific}$ is set to be constant for all domains. The proportion of electrode area attributed to a domain S_{domain} and the specific gas liquid interface $S_{phase\ interface}$ of each domain have been adjusted individually to reproduce the measurements.

The model was implemented in Matlab. Measured polarization curves (cf. Fig. 1) as well as impedance spectra (cf. Fig. 2) have been used for manual model parameter identification. The parameters were adjusted one by one in multiple iteration loops to minimize discrepancies between experiments and simulation results. The identified parameters values for non-distributed electrode properties are given in Table 3. The identified sizes and the specific gas-liquid interfaces for all ODC domains are given in Table 4. All constant model parameter are given in Table 5, all concentration-dependent parameters are given in Table 6. The parameters and the model output are discussed in the next section.

5. Comparative model based analysis of inhomogeneous ODC

In Fig. 2a) the experimental and simulated impedance spectra are presented. The simulations reproduce the measurements well regarding the distorted shape of the semi-circles, the trend in charge transfer resistance with silver content (Fig. 2b)), and the time constant (Fig. 2c)). Additionally, in Fig. 1, the experimental and simulated polarization curves are given, which also agree with slight deviations in the range of very high and very low current densities. Deviations in the low current range may result from the change of the Tafel-slop at a overpotential of about 0.16V vs. OCP (IR-corrected) [8,26]. As discussed in [26], the reason for this behavior is not clear, possible reasons may be different adsorption isotherms of intermediates in low the potential region [49], or influences by electronic or ionic conductivities which also could lead to a change in Tafel-slope [50]. Even though the experimental setup is temperature-controlled [8], the electrode may heat up at high currents. This could explain the deviations in the higher current range. Moreover, it is possible that the inhomogeneities are not limited to an inhomogeneous electrolyte distribution. This may lead to effects not considered in the model. The model is additional validated against EIS spectra of the high performing ODC with 98 wt-% Ag at current densities of 1 kA m^{-2} and 4 kA m^{-2}. As shown in the appendix (Fig. 8) the simulation data agree well with the experimental impedance spectra in term of shape, time constant and charge transfer resistance. All in all, the presented model can describe the electrode behaviour reasonably well.

In the following, we will first discuss the influence of inhomogeneities on electrode performance by analysing the contributions of the representative electrode domains to the polarization curves. Subsequently, the influence of the inhomogeneities on the dynamic behaviour will be discussed by analysing the EIS spectra. The parameters of the individual ODC in Tables 3 and 4 are evaluated and compared in more detail during the analysis.

In Fig. 4, the individual contributions of the different domains towards the overall performance are shown for the ODC with 92 and 98 wt-% Ag.

The local current density of each domain is plotted versus the potential. In both ODC the representative domains strongly differ in their performance. For the ODC with 92 wt-% Ag, the current density in domain 1, which has the lowest electrolyte intrusion, approaches a plateau at around 0.5V, indicating a depletion of oxygen in the liquid phase. In contrast, the medium flooded domains 2 and 3, amounting to ca. 50 % of total electrode area, are most active and have not yet reached their limiting current density at 0.5 V vs. RHE. The highly flooded domains 4 and 5, amounting to ca. 40 % of electrode area, contribute only little to the total current density. Even though the ODC with 98 wt-% has comparable proportions of active regions, it reaches a significantly higher performance. To

Table 5
List of constant parameters and operating conditions.

Name	Symbol	Unit	Value
Operating conditions			
Pressure in gas chamber[a]	$P = P_{O_2}$	Pa	1.013×10^5
NaOH concentration in electrolyte bulk[a]	$c_{NaOH}(z = z_t)$	mol m^{-3}	9.68×10^3
H_2O concentration in electrolyte bulk [38]	$c_{H_2O}(z = z_t)$	mol m^{-3}	50.0×10^3
Temperature[a]	T	K	353.15
Electrochemical and kinetic data			
Charge transfer coefficient[b] [40]	α	–	0.15
Stoichiometric coefficient H_2O	$\nu_{H_2O}^{ORR}$	–	−2
Stoichiometric coefficient OH^-	ν_{OH}^{ORR}	–	+4
Open circuit potential [8]	E^0	V vs. RHE	1.13
Binary diffusion coefficients			
For gaseous oxygen/water [41]	$\mathscr{D}_{O_2,H_2O}^{gas}$	m^{2}s^{-1}	2.95×10^{-5}
For liquid oxygen/water[c] [41,42]	$\mathscr{D}_{O_2,H_2O}^{liq}$	m^{2}s^{-1}	2.18×10^{-9}
For liquid oxygen/NaOH[c] [41,42]	$\mathscr{D}_{O_2,NaOH}^{liq}$	m^{2}s^{-1}	3.25×10^{-9}
For liquid water/NaOH[d] [43]	$Ð_{H_2O,NaOH}^{liq}$	m^{2}s^{-1}	1.26×10^{-9}
Geometrical parameter			
Thin-film thickness [26]	z_{tf}	m	60×10^{-9}
Thickness of liquid diffusion layer[e] [25]	z_{ldl}	m	10×10^{-6}

[a] Experimental operating condition. [b] Measured with 6.5 M NaOH. [c] Calculated with modified Wilke and Chang equation, with $\Theta = 3.9$ and $a = 0.5$ chosen, adjusted to experimental data from Chatenet et al. [42]. [d] No NaOH data available, modeled for KOH with NaOH viscosity from Oisson et al. [44], described in [26]. [e] Estimated to be independent of current density. Taken from our previous study where it was identified to be $10\,\mu m$ for measurements with horizontally orientated ODC [25], the measurement results in the set-up used here correspond to those in the reference cell [8].

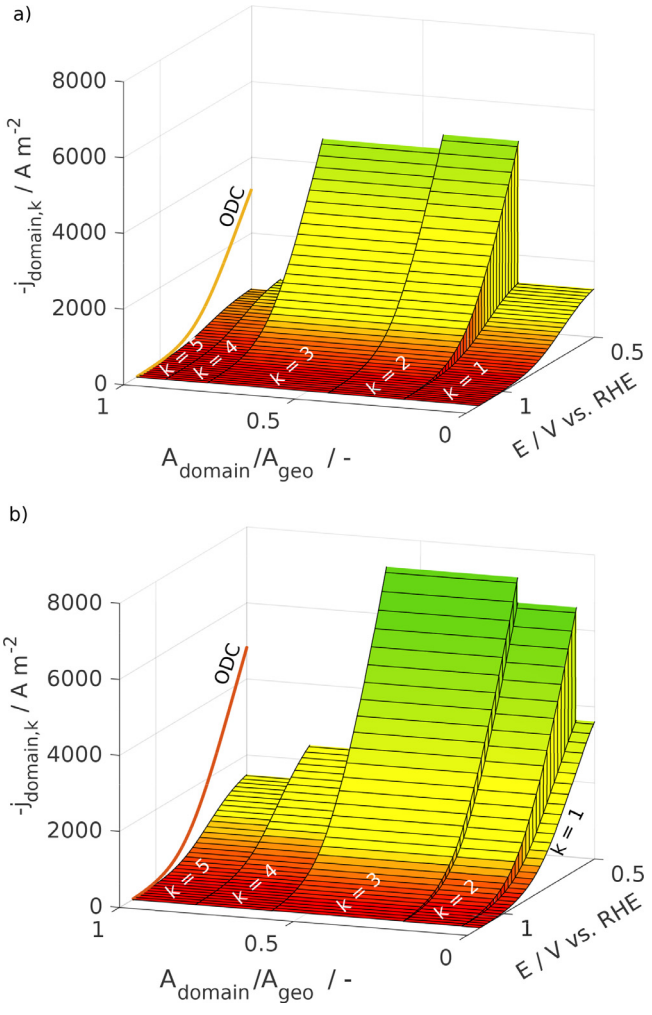

Fig. 4. Simulated current density dependent on the potential in each domain k and for total ODC, for ODC with a) 92 wt-% Ag and b) 98 wt-% Ag.

Table 6
Electrolyte concentration-dependent variables.

Name	Symbol	Unit
Inverse Henry constant[a] [5]	H_{O_2}	Pa m^{3}mol^{-1}
Activity coefficient of O_2[b] [45]	γ_{O_2}	-
Activity of H_2O [46]	a_{H_2O}	-
Mean activity coefficient of NaOH [47]	$\gamma_{\pm}$	kg mol^{-1}
Density of electrolyte [44]	ρ	kg m^{-3}
Water vapor pressure [38]	$p_{H_2O}^{vap}$	Pa

[a] Extrapolated from $c_{NaOH} \leq 6M$, but as shown in [48] extrapolated values fit very well to experiments with $c_{NaOH} \leq 12M$. [b] Extrapolated from $c_{NaOH} \leq 5.5M$, but as shown in original research, calculations for e.g. $c_{KOH} \leq 13.5M$ are valid [45].

understand this discrepancy in performance between the two ODC and their different domains, the differences of electrolyte intrusion as well as the gas-liquid interface have to be taken into account. In Fig. 5a), the proportion of the pore volume that is filled with electrolyte, p_v, is displayed over the dimensionless electrode thickness for all ODC. The proportion is calculated according to Fig. 3a) by accumulating the relative sizes of the domains k, which is equal to the relative volume fraction of the respective domains, that are flooded at a respective location. We assume that pores are flooded to different degrees in the three-phase zone. For the calculation we use an average degree of 50 % flooding since no further information on the degree of flooding in the three phase area is available. Thus, only half of the relative size of the domain is taken into account if the three-phase area is present at the respective location. Eq. (47) describes the calculation of the electrolyte filling over the electrode depth, z_d is the distance from the end of the electrode facing the liquid diffusion layer:

$$p_v(z_d) = \begin{cases} \sum_{k=1}^{1} S_{domain,k} - 0.5 \cdot S_{domain,1} & \text{for } z_d < 0.01 \cdot z_l \\ \sum_{k=1}^{2} S_{domain,k} - 0.5 \cdot S_{domain,2} & \text{for } 0.01 \cdot z_l \leq z_d < 0.032 \cdot z_l \\ \dots & \dots \\ \sum_{k=1}^{5} S_{domain,k} - 0.5 \cdot S_{domain,5} & \text{for } 0.316 \cdot z_l \leq z_d < z_l \end{cases} \tag{47}$$

Among the electrodes a trend of decreasing electrolyte saturation with higher PTFE content is clearly visible. This agrees with the

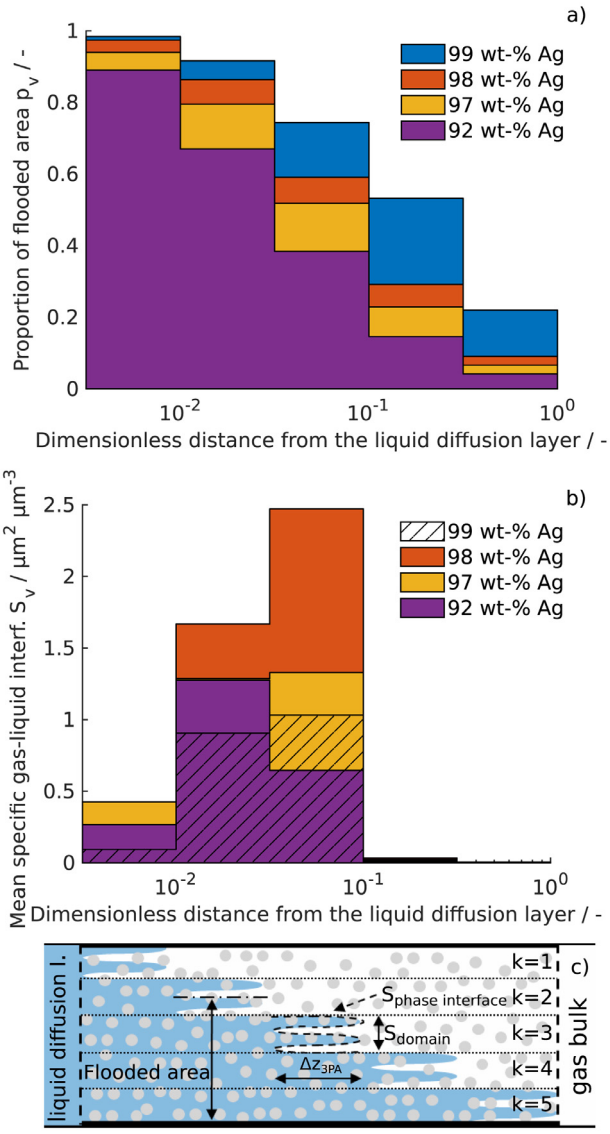

Fig. 5. Identified properties of ODC with different Ag-content: a) Electrolyte distribution dependent on the dimensionless location within the gas diffusion electrode (calculated by Eq. (47)); b) average area of gas-liquid interface per electrode volume dependent on the dimensionless location within the gas diffusion electrode (calculated by Eq. (48)); c) Schematic illustration of the electrolyte intrusion and gas-liquid interface distribution for reference.

results of a radiographic study of Paulisch et al. on similar electrodes, who found that a higher Ag content leads to a higher electrolyte saturation [9]. The effect can be attributed to the hydrophobic properties of the PTFE. According to our simulation results, also the porosity of the ODC decreases with increasing PTFE content – this trend agrees qualitatively with FIB/SEM analyses of ODC with varying Ag amount [8]. The porosity change may have an additional effect on the wettability of the electrodes as smaller pore diameters cause higher capillary forces. Although the wetted catalyst surface is the largest in the 99 wt-% Ag, this ODC has the lowest performance. This is interpreted as an indication that the actual electrochemical reaction rate is not the performance limiting step, even at medium current densities. The poor solubility of oxygen in liquid electrolytes is a well-known phenomenon [5]. Therefore the size of the gas-liquid interface can limit the performance. With the simulation data, an estimation of the size of the interface dependent on the location within the ODC has been made, which is given in Fig. 5b). The specific area of the gas-liquid interface within a given volume at each location z_d is calculated by scaling the specific gas-liquid interfaces of the respective domains according to their share of the total electrode area (eq. 48):

$$S_v(z_d) = \begin{cases} \frac{S_{\text{phase interface},1}}{\Delta z_{3PA,1}} \cdot S_{\text{domain},1} & \text{for } z_d < 0.01 \cdot z_l \\ \frac{S_{\text{phase interface},2}}{\Delta z_{3PA,2}} \cdot S_{\text{domain},2} & \text{for } 0.01 \cdot z_l \le z_d < 0.032 \cdot z_l \\ \dots & \dots \\ \frac{S_{\text{phase interface},5}}{\Delta z_{3PA,3}} \cdot S_{\text{domain},5} & \text{for } 0.316 \cdot z_l \le z_d < z_l \end{cases} \tag{48}$$

According to Fig. 5b), the ODC with 98 wt-% Ag exhibits the largest gas-liquid interface and – as the reaction mostly takes place close to the phase interface – this electrode has thus the largest active three-phase region and the lowest charge transfer resistance. This causes the high current densities presented in Fig. 4b). It seems that the electrode composition of 98 wt-% Ag and 2 wt-% PTFE leads to an optimal balance between hydrophilic and hydrophobic properties and thus the highest performance. In contrast, the ODC with 99 wt-% Ag is highly flooded so that the low performance can be attributed to missing gas phase. On the other side, the ODC with 92 wt-% Ag is barely flooded. Thus the gas-liquid interface is too small due to insufficient electrolyte intrusion. Furthermore, the model suggests what would be intuitively expected: Stronger hydrophobic properties of the electrodes lead to a shift of the three-phase boundaries towards the gas side. Almost the full gas-liquid interface, and thus active area, is located within the first 10% of the electrode from the liquid side whereas much of the Ag electrode at the gas side is not electrochemically active. This also suggests that there is mostly a small distance only from the gas-liquid interface to the liquid bulk, and thus little mass transport resistance, which agrees with previous studies [25].

The claim of negligible mass transport limitation is also supported by the time constant analysis of the EIS measurements in Section 2. As presented in our previous publication, long mass transport ways in the liquid phase between the electrochemical active zone and the electrolyte reservoir lead to characteristic time constants [25]. Due to the fact that no mass transport time constants in any ODC were measured and due to the fact that the most flooded electrode with 99 wt-% Ag performs worst, we conclude that the flooded domains 4 and 5 of the ODC contribute very little to the total electrochemical activity. The conclusion that the highly flooded domains are inactive is counter intuitive, since in this domains both the gas phase and the liquid phase are present, thus the presence of a physical gas-liquid interface is expected (cf. Fig. 3) The electrochemical measurements as well as the macroscopic model strongly suggest that the three-phase areas in the middle of the ODC and close to the gas side are electrochemically almost "dead". To clarify the mechanism, further simulations on a pore scale or detailed experimental studies that link the electrode microstructure with the local performance would be necessary. Possible reasons for the low activity of largely flooded pores might be long mass transport ways across the ODC or bottlenecks in the pore system leading to a high ionic resistance. Perhaps also local salt accumulations due to the ORR [39] lead to a quasi insolubility of oxygen. The availability of oxygen affects the OCP and the reaction rate of the ORR. In fact, the here presented gas-liquid interface should be interpreted as the active interface of ionically and electrically well-connected pores with exposed silver surface, and not the physical gas-liquid interface.

We will now discuss the impact of inhomogeneities on EIS. Using the presented model, the different local electrolyte saturation

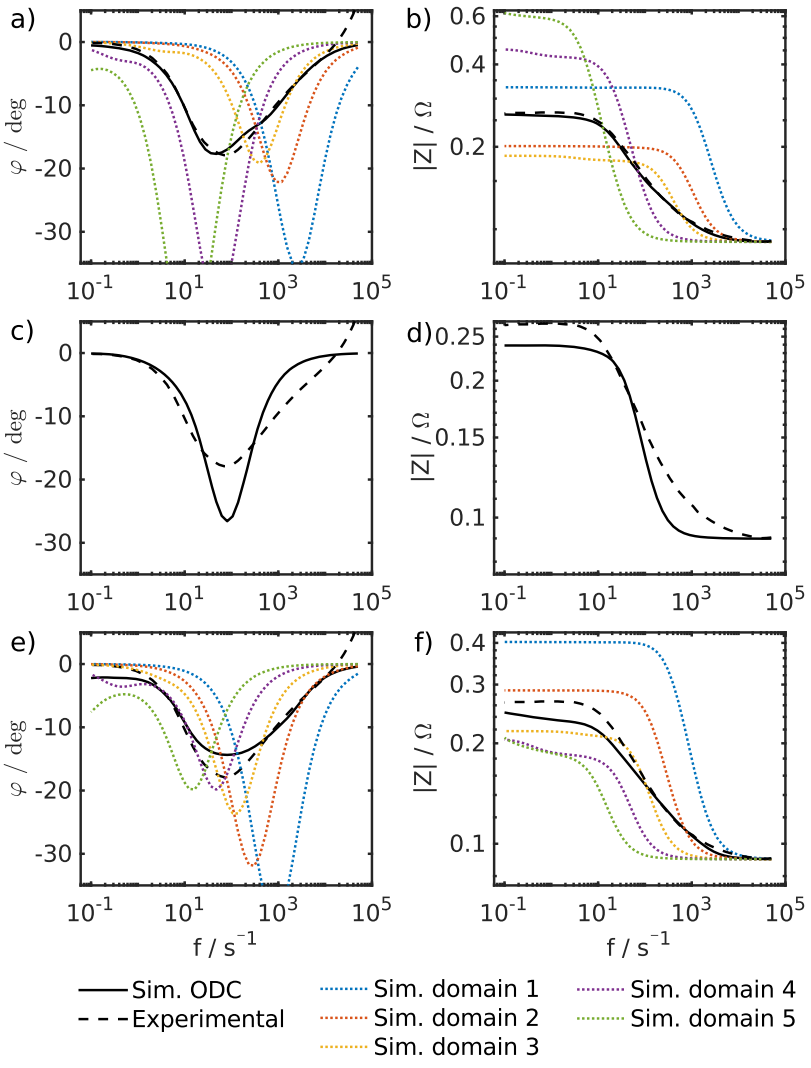

Fig. 6. Bode plots for EIS at $j = 2000$ A m^{-2} for ODC with 98 wt-% Ag for full electrode and single electrode domains. The three scenarios: a), b) inhomogeneous ODC (five domains); c), d) homogeneous ODC (one domain; $\frac{S_{\text{phase interface}}}{\Delta z_{3PA}} = 1.06\,\mu\text{m}^2\mu\text{m}^{-3}$); e), f) semi-homogeneous ODC (five domains, $\frac{S_{\text{phase interface}}}{\Delta z_{3PA}} = 6.4\,\mu\text{m}^2\mu\text{m}^{-3}$; $S^k_{\text{domain}} = 20$ %).

and the differences in local performance are shown to be responsible for the distorted shape of the semi-circles in the impedance spectra. The sinusoidal current of the total ODC is composed of the sinusoidal currents of all single domains. It represents the time constants and thus the phase shifts of all domains. The domains differ in double layer capacitance, in local performance, and thus in charge transfer resistance, therefore they all are characterized by their own time constant (cf. Eq. (5)). The impedance spectra can be examined in more detail by including the Bode plots, which are given for the example of the ODC with 98 wt-% Ag in Fig. 6a) and b). Besides the phase shift φ and impedance $|Z|$ of the entire ODC, the impedance values for the individual domains are also plotted separately.

The minima in phase shift of the domains extend over four orders of magnitude in frequency as shown in Fig. 6a). The phase shift φ at higher frequencies is governed by the less flooded domains (domains 1 and 2) and the more flooded domains (domain 4 and 5) govern the lower frequency range. The resulting overall phase shift curve reproduces the measurements well.

The model also is able to reproduce the trend of the EIS time constants over the Ag content which is evident in the experimental results. In Fig. 2b), it can be seen that the characteristic time constant is slightly increasing with the silver content in experiment and in simulation. The characteristic time constant equals the product of the double layer capacitance and the charge transfer resistance (cf. Eq. (5)). While R_{CT} from 92 to 99 wt-% Ag only increases by about a factor of 1.5, the time constant increases by a factor of 20 (cf. Fig. 2). A major part of the increase in the time constant can be attributed to an increase in double layer capacitance: Due to the more hydrophilic properties of the ODC with a higher Ag ratio, a higher part of the ODC is flooded, which leads to a larger share of wetted catalyst surface, where the double layer charge and discharge takes place. Additionally, the higher amount of silver catalyst within the ODC also results in a higher available total Ag surface area S_{cat}. This also explains, why the time constant of the ODC with 92 wt-% Ag is faster than the time constant of the ODC with 98 wt-% Ag although the charge transfer resistance increases. The identified double layer capacitances are within the range of previous studies [29].

As mentioned before, a slightly different shape of the EIS spectrum was observed for ODC with 99 wt-% Ag: The impedance spectrum shows a second, less pronounced semi-circle. According to the model results, the higher frequency semicircle can be assigned to the active pores, while the lower frequency semicircle is assigned to the flooded pores. In the remaining ODC, the

proportion of flooded pores is lower, so the impedance spectra of the flooded parts are less significant in the overall impedance spectra.

6. Model based scenario analysis of impedance spectra

As shown so far, the combination of dynamic and steady state electrochemical measurements and simulations enables to detect and quantify inhomogeneities and the related parameters in ODC, the influence of electrolyte distribution within gas diffusion electrodes on their electrochemical performance and dynamic behaviour is clearly visible. A methodology which can identify and quantify inhomogeneities is a highly promising tool that enables knowledge-driven, targeted design of electrodes and state diagnosis. To get deeper insights into effects of the parameter distributions and to evaluate the impedance spectra and polarization curves for their informative value and diagnostic capability regarding the electrolyte distribution, we present a scenario analysis in the following: Two hypothetical alternative model scenarios are analyzed for the high-performing ODC with 98 wt-% Ag, the results are compared with the above presented experimentally parameterised model for an ODC with 98 wt-% Ag. In the first scenario, a completely homogeneous ODC with only one domain is modeled: Here no influences due to an inhomogeneous electrolyte distribution are expected. The second scenario is an ODC with five domains with different degrees of flooding, where the flooding length z_{fa}^{k} is identical to that given in Table 2; however, we now assume equidistant domain areas and a constant specific gas-liquid interface over the whole electrode: $\frac{S_{\mathrm{phase\ interface}}}{\Delta z_{3\mathrm{PA}}} = 6.4\,\mu\mathrm{m}^2\,\mu\mathrm{m}^{-3}$ and $S_{\mathrm{domain}}^{k} = 20$ %. Here, the gas-liquid interface has the same surface area per electrode volume at each position in z-direction within the ODC, but the electrode maintains its different degrees of flooding. The model parameters for the two hypothetical scenarios are adjusted manually to best reproduce the polarization curve and the charge transfer resistance and time constant of the EIS. Model parameters and model characteristics are given in the appendix.

The outcome of the scenario analysis is summarized in Fig. 7 where the simulated EIS spectra and polarization curves for all three scenarios are shown. All three model variations can reproduce the polarization curves, only minor differences between the model outputs are visible. However, in case of impedances, the simulated inhomogeneous ODC model matches the EIS spectra most accurately. In contrast, the homogeneous ODC shows a single non-distorted semicircle, while the ODC with semi-homogeneous properties exhibits a significant smaller impedance over the full frequency range up to 1 kHz, i.e. it has a lower charge transfer resistance. In addition, the model of a semi-homogeneous ODC shows signs of mass transport impacts, visible in the additional arc visible at low frequencies below 1 Hz.

The underlying effects can be explained on the basis of the Bode diagrams. In Fig. 6c) and d) the Bode plot for the homogeneous ODC is illustrated. It can be seen that the minimum in phase shift is spread over approximately two orders of magnitudes in frequency. The phase shift curve is clearly not as wide as the measured phase shift, since a distribution of time constants is missing. The semi-homogeneous ODC features a phase shift over a wide frequency range (Fig. 6e)). However, its phase shift as well as the impedance (Fig. 6f)) of the semi-homogeneous ODC diverge from the measurements at frequencies below 1 Hz, i.e. where mass transport effects would be expected. It can be seen from the lower magnitude of the impedance $|Z|$ that the highly flooded domains both 4 and 5 exhibits a small $|Z|$ and thus contribute significantly to the total current. In these domains, the mass transport length of the liquid electrolyte within the ODC is so long that we can observe a time constant of the water and hydroxide ion

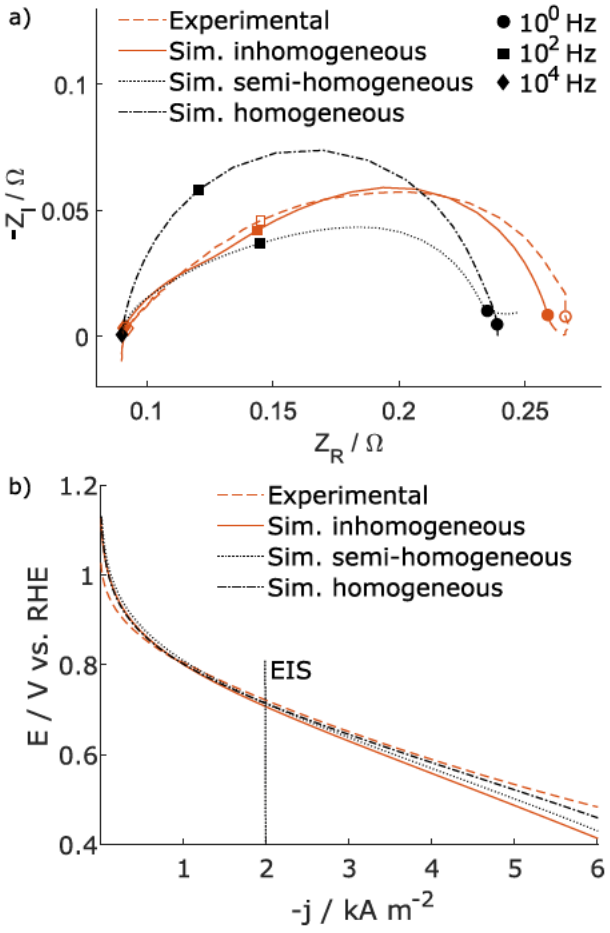

Fig. 7. Experimental and different simulated scenarios: a) EIS at $j = 2000\mathrm{A\ m^{-2}}$ for ODC with 98 wt-% Ag, b) polarization curve.

mass transport at frequencies below 1Hz. This results in overlapping mass transport semi-circles of the highly flooded domains 4 and 5 that form the peculiar almost horizontal line in the Nyquist diagram. Please note that due to the defined diffusion length no Warburg-type behavior is expected. As previously discussed, as a mass-transport related behavior is not visible in the experimental data, it can be concluded that such a semi-homogeneous condition is not present in the experimental analyzed electrodes.

Concluding, although all scenarios match the steady state data, only the inhomogeneous model can reproduce the impedance spectra. The homogeneous electrolyte distribution does not meet the distorted semi-circles; the semi-homogeneous of the electrolyte exhibits an additional time constant due to the active regions close the end of the ODC facing the gas side. The ability of EIS for detecting time constant and their distributions implies that dynamic electrochemical methods are a suitable tool for investigating and quantifying the gas-liquid distribution in gas diffusion electrodes and its impact on the electrode performance.

7. Conclusions

In this work we investigated the influence of electrolyte distribution for ODC with different binder-silver ratios on electrode performance and electrode dynamics using experimental as well as modeled polarization curves and impedance spectra. Experimental impedance spectra of oxygen depolarized cathodes with different Ag- and PTFE-content have been presented which were mainly characterized by fast time constants of $\tau \leq 0.03$ s and dis-

torted semi-circles in the Nyquist plot. For a deeper understanding of the impedance spectra, we present the first model of an ODC with distributed properties. The fast time constants can be assigned to the double layer charge and discharge, whereas the distorted semi-circles are a result of locally varying electrolyte intrusion depth. The model results suggest that pore systems with a low electrolyte intrusion makes a significantly higher contribution to the total performance than the highly flooded pores. A comparative model-based analysis of ODC with different silver to PTFE ratios has shown that the electrodes differ significantly in performance and dynamics. Performance is not attributed to a large wetted catalyst surface but to a large active gas-liquid interface that is located close to the electrolyte bulk. Furthermore, the model results were compared with two hypothetical scenarios of a homogeneous ODC and an ODC active over the entire electrode thickness. It was shown that the homogeneous ODC exhibits undistorted semi-circles, whereas the electrode with the semi-homogeneous gas-liquid interface shows mass transport effects, which are both not visible in the experimental impedance spectra.

The presented insight will aid experimentalists and electrode designers to better diagnose the state of their electrode using EIS and to judge how heterogeneous or well distributed the electrolyte phase is. EIS will also help to monitor electrodes: As electrodes age, their hydrophobicity might change and thus electrolyte distribution, EIS and performance. Future studies are needed to investigate the local performance and the structure on a pore-scale level and to establish a direct link between the microstructure and ODC performance.

Declaration of Competing Interest

The authors declare that they have no known competing financial interests or personal relationships that could have appeared to influence the work reported in this paper.

Credit authorship contribution statement

Maximilian Röhe: Conceptualization, Methodology, Software, Validation, Formal analysis, Data Curation, Writing - original draft. **David Franzen:** Formal analysis, Investigation, Data Curation, Writing - review & editing. **Fabian Kubannek:** Conceptualization, Methodology, Formal analysis, Writing - review & editing, Funding acquisition. **Barbara Ellendorff:** Resources, Writing - review & editing. **Thomas Turek:** Formal analysis, Writing - review & editing, Supervision, Funding acquisition, Project administration. **Ulrike Krewer:** Conceptualization, Methodology, Formal analysis, Writing - review & editing, Supervision, Funding acquisition, Project administration.

Acknowledgments

The authors are thankful to the Deutsche Forschungsgemeinschaft (DFG) for funding this research in the framework of the Forschungsgruppe “Multi-scale analysis of complex three-phase systems: oxygen reduction on gas-diffusion electrodes in aqueous electrolyte” (FOR 2397-2; research grants KR 3850/6-2 and TU 89/13-2). Further thanks are addressed to Marco Heinrich for helping to interpret the impedance spectra.

Appendix A. EIS at different current densities

We validated the model additional against EIS spectra of the ODC with 98 wt-% Ag (ODC with highest performance) at current densities of 1 kA m^{-2} and 4 kA m^{-2}. As presented earlier, the double layer capacitance in ODC is dependent on the cell potential or the current density respectively [29]. Since this effect is important for the comparison of the impedance spectra at different current densities, we have adjusted the double-layer capacitances for the simulations with 1 and 4 kA m^{-2} according to the in [29] measured relations, all further simulation parameters have not been changed:

- $C_{dl,cat}(j = 1\ \text{kA m}^{-2}) \approx 1.3 \cdot C_{dl,cat}(j = 2\ \text{kA m}^{-2})$
- $C_{dl,cat}(j = 4\ \text{kA m}^{-2}) \approx 0.6 \cdot C_{dl,cat}(j = 2\ \text{kA m}^{-2})$

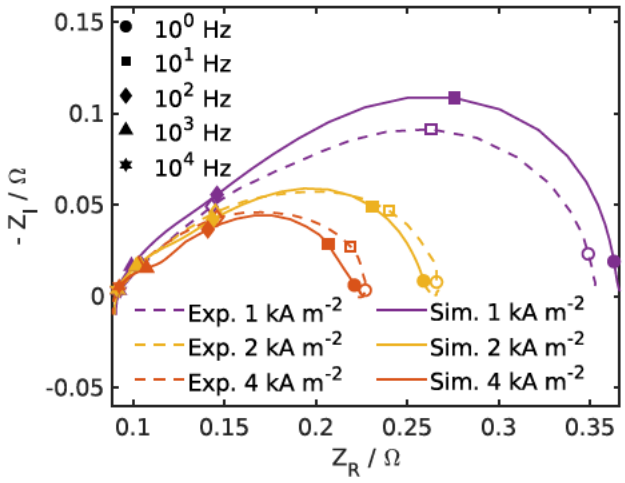

Fig. 8. Simulated and experimental EIS at different current densities of ODC with 98 wt-% Ag.

Measurement and simulation results for different current densities are shown in Fig. 8. The simulation data agree well with the experimental impedance spectra in term of shape, time constant and charge transfer resistance. Both, the measurements as well as the simulations, indicate a acceleration of the time constant with increasing current density. The simulation data show that at all current densities the time constant is dominated by double layer charge and discharge.

Appendix B. Model parameters of the scenario analysis

Please note that the discussed scenarios are hypothetical and based on divergent assumptions. The reaction rate (Eq. (7)) of the ORR and the charge balance (Eq. (14)) are functions of the wetted catalyst area. Since the amount of flooded pores and thus the wetted catalyst area are varied in the scenarios, the double layer capacitance and the reaction rate constant have been readjusted to reproduce the measured current densities and time constants.

Semi-homogeneous

- Number of domains: 5
- Specific domain area: Constant for all domains, $S^k_{\text{domain}} = const. = 20\ \%$
- Specific gas liquid interface: $\frac{S_{\text{phase interface}}}{\Delta z_{3PA}} = const. = 6.4\,\mu\text{m}^2\,\mu\text{m}^{-3}$
- Δz_{3PA} and z^k_{fa} according to Table 2.

Homogeneous

- Number of domains: 1
- Specific gas liquid interface: $\frac{S_{\text{phase interface}}}{\Delta z_{3PA}} = const. = 1.06\,\mu\text{m}^2\,\mu\text{m}^{-3}$, the three-phase area is located directly at the liquid side of the ODC with $\Delta z_{3PA} = 34\,\mu\text{m}$.

All further parameters are given in Table 7.

Table 7
Parameters identified from electrochemical experiments and ODC model for ODC with 98 wt-% Ag with hypothetical scenarios.

Name	Symbol	Unit	Semi-homogeneous	Homogeneous
Reaction rate constant	$k_{0,cat}$	mol $m^{-2}s^{-1}$	0.28	0.51
Double layer capacitance	$C_{dl,cat}$	F m^{-2}	3.04	5.21
Porosity[a]	ε	–	0.4	
Specific catalyst interface[a]	S_{cat}	$\mu m^2 \mu m^{-3}$	0.79	
Specific resistance[a,b]	$R_{specific}$	$\Omega\, m^2$	2.83×10^{-5}	

[a] Same parameter value as identified for the inhomogeneous modeled ODC. [b] High frequency resistance from EIS measurements [8].

References

[1] F. Kubannek, T. Turek, U. Krewer, Modeling oxygen gas diffusion electrodes for various technical applications, Chemie Ingenieur Technik 91 (6) (2019) 720–733, doi:10.1002/cite.201800181.

[2] J. Kintrup, M. Millaruelo, V. Trieu, A. Bulan, E.S. Mojica, Gas diffusion electrodes for efficient manufacturing of chlorine and other chemicals, Electrochem. Soc. Interface 26 (2) (2017) 73–76, doi:10.1149/2.F07172if.

[3] M. Chatenet, L. Genies-Bultel, M. Aurousseau, R. Durand, F. Andolfatto, Oxygen reduction on silver catalysts in solutions containing various concentrations of sodium hydroxide - Comparison with platinum, J. Appl. Electrochem. 32 (10) (2002) 1131–1140, doi:10.1023/A:1021231503922.

[4] I. Moussallem, J. Jörissen, U. Kunz, S. Pinnow, T. Turek, Chlor-alkali electrolysis with oxygen depolarized cathodes: history, present status and future prospects, J. Appl. Electrochem. 38 (9) (2008) 1177–1194, doi:10.1007/s10800-008-9556-9.

[5] D. Tromans, Modeling oxygen solubility in water and electrolyte solutions, Ind. Eng. Chem. Res. 39 (3) (2000) 805–812, doi:10.1021/ie990577t.

[6] M. Röhe, F. Kubannek, U. Krewer, Processes and their limitations in oxygen depolarized cathodes: a dynamic model–based analysis, ChemSusChem 11 (2019) 2373–2385, doi:10.1002/cssc.201900312.

[7] R. Kuwertz, I.G. Martinez, T. Vidaković-Koch, K. Sundmacher, T. Turek, U. Kunz, Energy-efficient chlorine production by gas-phase HCl electrolysis with oxygen depolarized cathode, Electrochem. Commun. 34 (2013) 320–322, doi:10.1016/j.elecom.2013.07.035.

[8] D. Franzen, B. Ellendorff, M.C. Paulisch, A. Hilger, M. Osenberg, I. Manke, T. Turek, Influence of binder content in silver-based gas diffusion electrodes on pore system and electrochemical performance, J. Appl. Electrochem. 49 (7) (2019) 705–713, doi:10.1007/s10800-019-01311-4.

[9] M.C. Paulisch, M. Gebhard, D. Franzen, A. Hilger, M. Osenberg, N. Kardjilov, B. Ellendorff, T. Turek, C. Roth, I. Manke, Operando laboratory x-ray imaging of silver-based gas diffusion electrodes during oxygen reduction reaction in highly alkaline media, Materials 12 (17) (2019), doi:10.3390/ma12172686.

[10] P. Kunz, M. Hopp-Hirschler, U. Nieken, Simulation of electrolyte imbibition in gas diffusion electrodes, Chemie Ingenieur Technik 91 (6) (2019) 883–888, doi:10.1002/cite.201800202.

[11] S. Tsushima, K. Teranishi, K. Nishida, S. Hirai, Water content distribution in a polymer electrolyte membrane for advanced fuel cell system with liquid water supply, Magn. Reson. Imaging 23 (2 SPEC. ISS.) (2005) 255–258, doi:10.1016/j.mri.2004.11.059.

[12] P. Krüger, H. Markötter, J. Haußmann, M. Klages, T. Arlt, J. Banhart, C. Hartnig, I. Manke, J. Scholta, Synchrotron X-ray tomography for investigations of water distribution in polymer electrolyte membrane fuel cells, J. Power Sources 196 (12) (2011) 5250–5255, doi:10.1016/j.jpowsour.2010.09.042.

[13] B. Tavakoli, R. Roshandel, The effect of fuel cell operational conditions on the water content distribution in the polymer electrolyte membrane, Renew. Energy 36 (12) (2011) 3319–3331, doi:10.1016/j.renene.2011.05.003.

[14] U. Krewer, F. Röder, E. Harinath, R.D. Braatz, B. Bedürftig, R. Findeisen, Dynamic models of Li-Ion batteries for diagnosis and operation: a review and perspective, J. Electrochem. Soc. 165 (16) (2018) A3656–A3673, doi:10.1149/2.1061814jes.

[15] U. Krewer, T. Vidakovic-Koch, L. Rihko-Struckmann, Electrochemical oxidation of carbon-containing fuels and their dynamics in low-temperature fuel cells, ChemPhysChem 12 (14) (2011) 2518–2544, doi:10.1002/cphc.201100095.

[16] U. Krewer, H.-K. Yoon, H.-T. Kim, Basic model for membrane electrode assembly design for direct methanol fuel cells, J. Power Sources 175 (2) (2008) 760–772, doi:10.1016/j.jpowsour.2007.09.115.

[17] Q. Mao, U. Krewer, Sensing methanol concentration in direct methanol fuel cell with total harmonic distortion: theory and application, Electrochim. Acta 68 (2012) 60–68, doi:10.1016/j.electacta.2012.02.018.

[18] M.D. Levi, C. Wang, D. Aurbach, Two parallel diffusion paths model for interpretation of PITT and EIS responses from non-uniform intercalation electrodes, J. Electroanal. Chem. 561 (2004) 1–11, doi:10.1016/j.jelechem.2003.07.014.

[19] K. Jüttner, W. Lorenz, Electrochemical impedance spectroscopy (EIS)of corrosion processes on inhomogeneous surfaces, Mater. Sci. Forum 44-45 (1991) 191–204. 10.4028/ www.scientific.net/msf.44-45.191.

[20] S. Chevalier, B. Auvity, J.C. Olivier, C. Josset, D. Trichet, M. Machmoum, Detection of cells state-of-health in PEM fuel cell stack using EIS measurements coupled with multiphysics modeling, Fuel Cells 14 (3) (2014) 416–429, doi:10.1002/fuce.201300209.

[21] U. Krewer, A. Kamat, K. Sundmacher, Understanding the dynamic behaviour of direct methanol fuel cells: response to step changes in cell current, J. Electroanal. Chem. 609 (2) (2007) 105–119, doi:10.1016/j.jelechem.2007.06.015.

[22] I. Moussallem, S. Pinnow, N. Wagner, T. Turek, Development of high-performance silver-based gas-diffusion electrodes for chlor-alkali electrolysis with oxygen depolarized cathodes, Chem. Eng. Process. 52 (2012) 125–131, doi:10.1016/j.cep.2011.11.003.

[23] M. Neumann, M. Osenberg, A. Hilger, D. Franzen, T. Turek, I. Manke, V. Schmidt, On a pluri-Gaussian model for three-phase microstructures, with applications to 3D image data of gas-diffusion electrodes, Comput. Mater. Sci. 156 (September 2018) (2019) 325–331, doi:10.1016/j.commatsci.2018.09.033.

[24] M.E. Orazem, B. Tribollet, Electrochemical Impedance Spectroscopy, Wiley, Hoboken, New Jersey, 2008, doi:10.1002/9780470381588.

[25] M. Röhe, A. Botz, D. Franzen, F. Kubannek, B. Ellendorff, D. Öhl, W. Schuhmann, T. Turek, U. Krewer, The key role of water activity for the operating behavior and dynamics of oxygen depolarized cathodes, ChemElectroChem 6 (22) (2019) 5671–5681, doi:10.1002/celc.201901224.

[26] S. Pinnow, N. Chavan, T. Turek, Thin-film flooded agglomerate model for silver-based oxygen depolarized cathodes, J. Appl. Electrochem. 41 (9) (2011) 1053–1064, doi:10.1007/s10800-011-0311-2.

[27] X. Zhong, M. Schulz, C.H. Wu, M. Rabe, A. Erbe, M. Rohwerder, Limiting current density of oxygen reduction under ultrathin electrolyte layers: from the micrometer range to monolayers, ChemElectroChem 8 (4) (2021) 712–718, doi:10.1002/celc.202100083.

[28] T. Muzaffar, T. Kadyk, M. Eikerling, Tipping water balance and the Pt loading effect in polymer electrolyte fuel cells: a model-based analysis, Sustain. Energy Fuels 2 (6) (2018) 1189–1196, doi:10.1039/c8se00026c.

[29] G.D. Polcyn, Charakterisierung und Modellierung der Sauerstoffreduktion an Sauerstoff-Verzehr-Kathoden für die Chlor-Alkali-Elektrolyse anhand von Abschaltmessungen, Dissertation, Technische Universität Dortmund, 2018.

[30] B.B. Blizanac, P.N. Ross, N.M. Markovic, Oxygen electroreduction on Ag(1 1 1): the pH effect, Electrochim. Acta 52 (6) (2007) 2264–2271, doi:10.1016/j.electacta.2006.06.047.

[31] Z. Lukács, The numerical evaluation of the distortion of EIS data due to the distribution of parameters, J. Electroanal. Chem. 432 (1–2) (1997) 79–83, doi:10.1016/S0022-0728(97)00217-9.

[32] A. Schröder, K. Wippermann, W. Lehnert, D. Stolten, T. Sanders, T. Baumhöfer, N. Kardjilov, A. Hilger, J. Banhart, I. Manke, The influence of gas diffusion layer wettability on direct methanol fuel cell performance: a combined local current distribution and high resolution neutron radiography study, J. Power Sources 195 (15) (2010) 4765–4771, doi:10.1016/j.jpowsour.2010.02.057.

[33] A.A. Kulikovsky, J. Divisek, A.A. Kornyshev, Modeling the cathode compartment of polymer electrolyte fuel cells: dead and active reaction zones, J. Electrochem. Soc. 146 (11) (1999) 3981–3991, doi:10.1149/1.1392580.

[34] S. Kandaswamy, A. Sorrentino, S. Borate, L.A. Živković, M. Petkovska, T. Vidaković-Koch, Oxygen reduction reaction on silver electrodes under strong alkaline conditions, Electrochim. Acta 320 (2019) 134517, doi:10.1016/j.electacta.2019.07.028.

[35] B.B. Blizanac, P.N. Ross, N.M. Marković, Oxygen reduction on silver low-index single-crystal surfaces in alkaline solution: rotating ring $disk_{(/Ag(hkl))}$ studies, J. Phys. Chem.(10) 4735–4741. 10.1021/jp056050d

[36] B. Kögl, Grundlagen der Verfahrenstechnik, Springer Vienna, Vienna, 1981, doi:10.1007/978-3-7091-2270-9.

[37] R.B. Bird, D.J. Klingenberg, Multicomponent diffusion – a brief review, Adv. Water Resources 62 (2013) 238–242, doi:10.1016/j.advwatres.2013.05.010.

[38] H.G. Hirschberg, Handbuch Verfahrenstechnik und Anlagenbau, Springer-Verlag Berlin Heidelberg New York, 1999, doi:10.1007/978-3-642-58357-5.

[39] A. Botz, J. Clausmeyer, D. Öhl, T. Tarnev, D. Franzen, T. Turek, W. Schuhmann, Local activities of hydroxide and water determine the operation of silver-based oxygen depolarized cathodes, Angewandte Chemie Int. Ed. 57 (2018) 12285–12289, doi:10.1002/anie.201807798.

[40] P.K. Adanuvor, Oxygen reduction on silver in 6.5M caustic soda solution, J. Electrochem. Soc. 135 (10) (1988) 2509, doi:10.1149/1.2095367.

[41] B.E. Poling, J. Prausnitz, J. O'Connell, The Properties of Gases and Liquids, McGraw Hill professional, McGraw-Hill Education, 2000.

[42] M. Chatenet, M. Aurousseau, R. Durand, Comparative methods for gas diffusivity and solubility determination in extreme media: application to molecular

oxygen in an industrial chlorine-soda electrolyte, Ind. Eng. Chem. Res. 39 (8) (2000) 3083–3089, doi:10.1021/ie000044g.
[43] J. Newman, D. Bennion, C.W. Tobias, Mass transfer in concentrated binary electrolytes, Berichte der Bunsengesellschaft für physikalische Chemie 69 (1965) 608–612. 10.1002
[44] J. Oisson, I.A. Jernqvist, G.I. Aly, Thermophysical properties of aqueous NaO-H-H_2O solutions at high concentrations, Int. J. Thermophys. 18 (3) (1997).
[45] S.L. Clegg, P. Brimblecombe, The solubility and activity coefficient of oxygen in salt solutions and brines, Geochimica et Cosmochimica Acta 54 (4) (1990) 3315–3328.
[46] G. Åkerlöf, G. Kegeles, Thermodynamics of concentrated aqueous solutions of sodium hydroxide, J. Am. Chem. Soc. 62 (3) (1940) 620–640, doi:10.1021/ja01860a057.
[47] J. Balej, Activity coefficients of aqueous solutions of NaOH and KOH in wide concentration and temperature ranges, Collect. Czechoslovak Chem. Commun. 61 (1996) 1549–1562.
[48] C. Zhang, F.R.F. Fan, A.J. Bard, Electrochemistry of oxygen in concentrated NaOH solutions: Solubility, diffusion coefficients, and superoxide formation, J. Am. Chem. Soc. 131 (1) (2009) 177–181, doi:10.1021/ja8064254.
[49] D.B. Sepa, M.V. Vojnovic, L.M. Vracar, A. Damjanovic, Apparent enthalpies of activation of electrodic oxygen reduction at platinum in different current density regions-II. Alkaline solution, Electrochim. Acta 31 (1) (1986) 97–101, doi:10.1016/0013-4686(86)80068-8.
[50] J.N. Soderberg, A.C. Co, A.H. Sirk, V.I. Birss, Impact of porous electrode properties on the electrochemical transfer coefficient, J. Phys. Chem. B 110 (21) (2006) 10401–10410, doi:10.1021/jp060372f.